

## PAPERS

# Study on Ag mesh/conductive oxide hybrid transparent electrode for film heaters

To cite this article: Namyong Kwon *et al* 2014 *Nanotechnology* **25** 265702

View the [article online](#) for updates and enhancements.

## Related content

- [Highly conductive and transparent Ag honeycomb mesh fabricated using a monolayer of polystyrene spheres](#)  
Namyong Kwon, Kyohyeok Kim, Sihyun Sung *et al*.
- [A cracked polymer templated Ag network for flexible transparent electrodes and heaters](#)  
Chaoting Zhu, Ruiqin Tan, Weijie Song *et al*.
- [Flexible transparent conductive films combining flexographic printed silver grids with CNT coating](#)  
Lixin Mo, Jun Ran, Li Yang *et al*.

## Recent citations

- [MetalBased Flexible Transparent Electrodes: Challenges and Recent Advances](#)  
Xi Lu *et al*
- [SilverNanowireEmbedded Photopolymer Films for Transparent Film Heaters with UltraFlexibility, Quick Thermal Response, and Mechanical Reliability](#)  
In Su Jin *et al*
- [Flexible biodegradable transparent heaters based on fractal-like leaf skeletons](#)  
Vipul Sharma *et al*



**RM5**  
Our confocal  
Raman Microscope.

Your Research. Our Expertise.

EDINBURGH  
INSTRUMENTS

edinst.com

The advertisement features a high-resolution image of the RM5 Confocal Raman Microscope. The microscope is shown from a side-on perspective, highlighting its compact design and various adjustment knobs. The background is dark with a subtle red glow, suggesting a scientific or laboratory setting. The text is prominently displayed in white and red, with the company logo and website address clearly visible.

# Study on Ag mesh/conductive oxide hybrid transparent electrode for film heaters

Namyong Kwon<sup>1</sup>, Kyohyeok Kim<sup>1</sup>, Jinhee Heo<sup>3</sup>, Insook Yi<sup>4</sup> and Ilsub Chung<sup>1,2</sup>

<sup>1</sup>SKKU Advanced Institute of Nanotechnology, Sungkyunkwan University, Suwon 440-746, Korea

<sup>2</sup>College of Information and Communication Engineering, Sungkyunkwan University, Suwon 440-746, Korea

<sup>3</sup>Korea Institute of Materials Science, Changwon, 641-831, Korea

<sup>4</sup>Advanced Technology Team, InkTec Technology Center, Ansan 425-839, Korea

E-mail: [ichung@skku.ac.kr](mailto:ichung@skku.ac.kr)


Received 3 March 2014, revised 27 April 2014

Accepted for publication 12 May 2014

Published 11 June 2014

## Abstract

Ag mesh-indium tin oxide (ITO) hybrid transparent conductive films were fabricated and evaluated for use in film heaters. PS monolayer templates were prepared using highly mono-dispersed PS spheres (11.2  $\mu\text{m}$ ) obtained by a filtering process with micro-sieves. At first, three Ag meshes with different sheet resistances (20, 100, and 300  $\Omega \text{sq}^{-1}$ ) and transmittances (70, 73, and 76%) were evaluated for film heaters in terms of voltage and long-term stability. Subsequently, in an effort to obtain better transmittance, Ag mesh-ITO hybrid heaters were fabricated utilizing finite ITO depositions. At the optimised ITO thickness (15 nm), the sheet resistance and the transmittance were 300  $\Omega \text{sq}^{-1}$  and 88%, respectively, which indicates that this material is a good potential candidate for an efficient defroster in vehicles.

 Online supplementary data available from [stacks.iop.org/NANO/25/265702/mmedia](http://stacks.iop.org/NANO/25/265702/mmedia)

Keywords: Ag mesh, ITO, film heater, transparent conductive film

(Some figures may appear in colour only in the online journal)

## 1. Introduction

Transparent conductive electrodes with a high optical transmittance and good electrical conductivity are essential for various applications, including solar cells, touch panels, light-emitting diodes (LEDs), and transparent heaters [1–10]. Amongst them, transparent heaters have attracted growing interest for a wide range of applications, such as vehicle window defrosters, mirrors, outdoor displays, and heat pads [4, 7–12]. In particular, since the vehicle window defroster is operated at 12 V, the lower resistance is an important factor to maximise desired attributes, including steady temperature and response time. Indium tin oxide (ITO) films have been used most often in transparent heaters. Even though an optimised trade-off between electrical resistivity and optical transparency has been obtained through more than 40 years of studies, a low power consumption efficiency and a slow thermal response with respect to the applied voltage are critical to

improving performance. There are many approaches that utilize alternative materials, such as metal nanowires [4, 5], conducting polymers [6, 7], carbon nanotube networks [8–10], graphene films [11, 12], hybrid thin films [13–17], and metal meshes [18–21].

Metal meshes are extremely conductive and can be produced in a roll-to-roll process for mass production. However, their relatively lower transmittance is a challenge that must be addressed for their successful application. In recent years, metal meshes with widths of less than 1  $\mu\text{m}$  have been reported; these were fabricated using the nanoimprint method or micro transfer moulding. However, their maximum transparency was below 80% (at 550 nm) [18]. On the other hand, a patterned metal mesh utilizing polystyrene (PS) spheres was also reported to replace transparent conductive films (TCFs) based on ITO films [19–21]. Wei *et al* reported a silver nanohole array with an optical transmittance of 65% and sheet resistance of 6  $\Omega \text{sq}^{-1}$  using PS spheres (300 nm in diameter)

as a mask [19]. Cheng *et al* fabricated an Au nanomesh with 72% transparency using PS spheres (600 nm in diameter) as an etching mask [20]. The larger mono-dispersed PS spheres were beneficial to yielding higher transparency [21]. Wang *et al* synthesised mono-dispersed PS microspheres with a diameter of  $7.09\ \mu\text{m}$  (coefficient of variation values less than 4.8%) using dispersion polymerisation [22]. However, it is difficult to synthesise mono-dispersed PS spheres larger than  $7\ \mu\text{m}$  in diameter for large-quantity production.

Recently, hybrid films have also been intensively studied to improve the electrical conductivity by embedding a thin metal film between ITO like a sandwich structure [16, 17]. Alford *et al* examined ITO/Ag/ITO (IMI) multilayers to improve the conductivity compared to ITO films. They found that most electrons had transported through the Ag film in ITO/Ag/ITO (IMI) multilayers because the resistivity of silver is much lower than that of ITO, thereby improving the sheet resistance [16]. In addition, Guillen *et al* also studied IMI multilayers on soda lime glass, where 10 nm Ag had been used as an intermediate metal layer between 30 nm ITO coatings [17]. However, the aforementioned studies still did not address the relatively lower transmittance.

In this study, we attempted to evaluate a new hybrid TCF heater, which consists of an Ag honeycomb mesh and ITO islands. We chose  $11.2\ \mu\text{m}$  PS spheres to fabricate various Ag mesh heaters with different sheet resistances (20, 100, and  $300\ \Omega\ \text{sq}^{-1}$ ) and transmittances (70, 73, and 76%). An Ag mesh heater with  $20\ \Omega\ \text{sq}^{-1}$  exhibited better performance in terms of a steady temperature characteristic up to  $100\ ^\circ\text{C}$  at 10 V, whilst that with  $300\ \Omega\ \text{sq}^{-1}$  revealed a steady temperature characteristic up to only  $38\ ^\circ\text{C}$  at the same voltage. However, to increase the transmittance of Ag mesh heaters, we further etched Ag meshes using chemicals and then deposited a small amount of ITO on these meshes to obtain hybrid Ag mesh heaters. Finally, we obtained good properties from the Ag mesh-ITO hybrid heaters in terms of transmittance (88%) and sheet resistance ( $300\ \Omega\ \text{sq}^{-1}$ ). We demonstrated a highly uniform temperature ( $43\ ^\circ\text{C}$ ) distribution at 12 V using the aforementioned Ag mesh-ITO hybrid heaters, which proved to be good candidates for efficient vehicle defrosters.

## 2. Experimental details

### 2.1. Formation of PS spheres

PS spheres with diameters ranging from approximately 3– $20\ \mu\text{m}$  were prepared by dispersion polymerisation. A 250 mL, three-neck, round-bottom flask was used, which was equipped with a reflux condenser, a nitrogen gas inlet, and a Teflon stirrer paddle. Styrene monomer (Sigma Aldrich, 64 g), 2,2'-azobisisobutyronitrile (AIBN, Sigma Aldrich, 0.64 g), polyvinyl-pyrrolidone (PVP K-30,  $M_w = 4.0 \times 10^4\ \text{g mol}^{-1}$ , Sigma Aldrich, 1.92 g), and ethanol (136 g) were used to obtain the aforementioned PS spheres. A styrene monomer was washed with a 2 M aqueous sodium hydroxide solution, distilled under reduced pressure to

remove the inhibitor and then stored in a refrigerator prior to use. The ethanol solution with dissolved PVP was poured into the reaction flask under a nitrogen atmosphere and stirred with a magnetic bar at 1300 rpm. Subsequently, another solution composed of styrene and AIBN was poured into the flask. The dispersion polymerisation was carried out for 24 h under a nitrogen gas ambient at  $70\ ^\circ\text{C}$ . The obtained PS microspheres were purified by means of centrifugation, decantation, and redispersion in sequence to remove the residual styrene and PVP.

### 2.2. Preparation of mono-dispersed PS spheres

PS spheres with an average diameter of  $11.2\ \mu\text{m}$  were obtained by filtering using two sieves (Stork Veco B.V.). The hole diameters of the sieves were  $10.3 \pm 0.2\ \mu\text{m}$  and  $12.2 \pm 0.2\ \mu\text{m}$ , respectively. As shown in figure S1 (available in the supporting information, at [stacks.iop.org/NANO/25/265702/mmedia](http://stacks.iop.org/NANO/25/265702/mmedia)), the filtering process was performed with a 5 wt% PS-ethanol solution under sonication. At first, PS spheres larger than  $12.2\ \mu\text{m}$  in diameter were filtered using a  $12.2\ \mu\text{m}$  sieve. Then, PS spheres smaller than  $10.3\ \mu\text{m}$  in diameter were eliminated using a  $10.3\ \mu\text{m}$  sieve, thereby yielding PS spheres ranging from  $10.3$  to  $12.2\ \mu\text{m}$  in diameter.

### 2.3. Fabrication of Ag mesh

First, a  $150\ \mu\text{m}$  thick poly(ethylene terephthalate) (PET) substrate was plasma-treated to obtain a hydrophilic surface (contact angle of  $\sim 50^\circ$ ). As explained in our previous study, the periodic hexagonal close-packed monolayer arrays composed of PS spheres were coated by a floating-transferring method [21]. Then, obtained PS templates were annealed at  $120\ ^\circ\text{C}$  for 3 min on a hot plate to reduce the parasitic Ag islands by shrinking the volume between the PS spheres and PET substrate. Ag ink (11.5 wt%, TEC-IJ-010, Inktec) was coated on a PS template using a bar-coater. Ag meshes were annealed at  $120\ ^\circ\text{C}$  for 3 min on a hot plate. Subsequently, a PS sphere monolayer film was lifted off by sonicating for 3 min in toluene. The additional Ag curing was performed at  $150\ ^\circ\text{C}$  for 5 min to improve the conductivity of the Ag mesh. Ag meshes were etched by immersing in nitric acid (20 wt%) to remove parasitic Ag islands. After wet etching, the sample was immersed in DI water and blown with nitrogen gas. Finally, Cu electrode plates were attached with silver paste to fabricate Ag mesh heaters. The length of each electrode was 3 cm, and the distance between the parallel electrodes was 4 cm.

### 2.4. Deposition of ITO layer

ITO films (50, 20, 15, and 10 nm) were deposited at room temperature using an rf-sputtering system. The ITO target was composed of  $\text{In}_2\text{O}_3$  containing 10 wt %  $\text{SnO}_2$ . The deposition rate was approximately  $3\ \text{\AA s}^{-1}$  at 1200 W. The desired thickness was obtained by controlling the deposition time. The base pressure was approximately  $1.25 \times 10^{-5}$  Torr, and ITO deposition was performed using pure Ar gas (99.999%)

with a flow rate of 100 SCCM (denotes standard cubic centimetres per minute at STP).

### 2.5. Characterisation

Images of PS spheres and Ag honeycomb meshes were obtained using field emission scanning electron microscopy (JSM-7401F, JEOL) equipped with an energy-dispersive x-ray spectrometer (EDS) system (Oxford INCA 350). Detailed morphological analyses of Ag honeycomb meshes were collected using a scanning probe microscope (SPA-300, Seiko Instruments) by probing with cantilevers (Si-DF40). The image-processing program (TOMORO SCOPE-EYE) was used to accurately analyse the dimensions of the PS spheres. In addition, sheet resistance and transmittance were obtained using a sheet resistance meter (FPP-2000, DASOL ENG) and transmittance meter (MTR-2, 3M), respectively. The voltages were applied across the two electrodes using a DC power supply (EDP-30015, PNCYS) for the heater test and then the current and the resistance of the heaters were measured simultaneously. Finally, the temperature of the heater was monitored using a thermal imaging camera (P640, FLIR).

## 3. Results and discussion

### 3.1. Filtered PS spheres

Figure 1(a) shows optical images obtained from the aforementioned sieves. The diameters of the holes were  $10.3 \pm 0.2 \mu\text{m}$  and  $12.2 \pm 0.2 \mu\text{m}$ , respectively. The distribution of filtered PS spheres given in figure 1(b) indicates that the average diameter of filtered PS spheres was about  $11.2 \mu\text{m}$ . In addition, the images provided in the inset of figure 1(b) clearly show uniform sizes. The coefficient of variation (CV) of the obtained PS spheres was measured as 4.8%, which is similar to that (3.8%) of the  $10 \mu\text{m}$  PS spheres obtained from Polyscience, Inc. The average diameter and CV of the PS spheres were calculated by measuring more than 400 individual spheres shown in field emission scanning electron microscopy (FE-SEM) images using an image-processing program (TOMORO SCOPE-EYE).

### 3.2. Ag mesh heater

Figure 2 illustrates schematic processes used to fabricate an Ag mesh heater using a PS sphere monolayer template. As described in the Experimental section, three samples were obtained using an Ag wet etching process. As wet etching processes were performed, a considerable number of parasitic Ag islands near Ag lines were removed, and the Ag lines were etched. As a result, Ag meshes with different sheet resistances and transmittances were obtained, as shown in figure 3. FE-SEM images shown in figure 3 represent three different etching times. Prior to wet etching, the sheet resistance of Ag mesh given in figure 3(a) was  $20 \Omega \text{sq}^{-1}$ , whilst the transmittance was 70%. After performing a wet etching process, the sheet resistance increased by 5 times ( $100 \Omega \text{sq}^{-1}$ ), whilst the transmittance increased only slightly from 70% to 73%, as

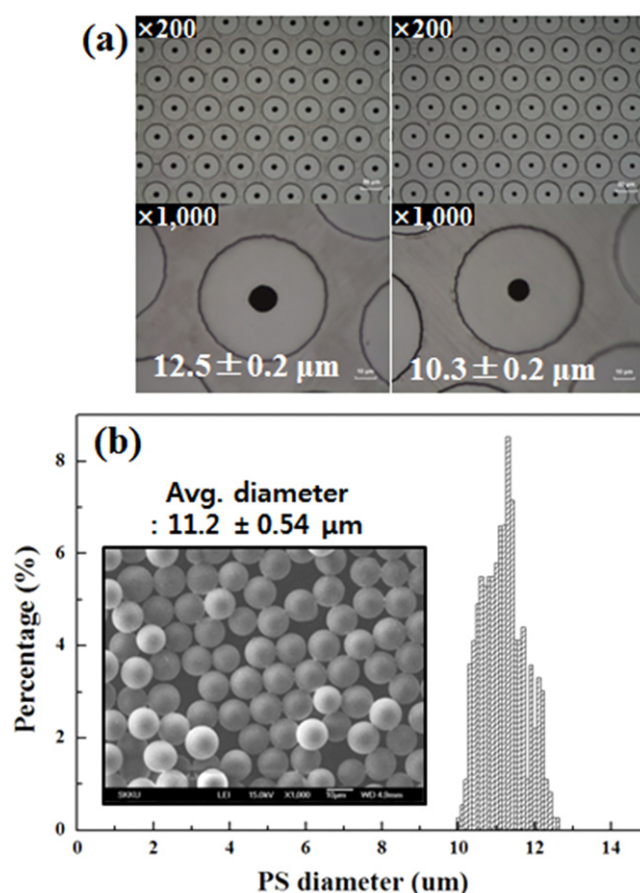


**Figure 1.** (a) Optical images of two sieves with holes with diameters of  $10.3 \pm 0.2 \mu\text{m}$  and  $12.2 \pm 0.2 \mu\text{m}$ . (b) Distribution of sieved PS spheres and optical images of highly mono-dispersed PS spheres with an average diameter of  $11.2 \mu\text{m}$ .

shown in figure 3(b). As indicated in figure 3(c), further wet etching increased the sheet resistance more than 10 times, whilst transmittance improves to only 76%. The summarised transmittances and sheet resistances of various samples are given in table 1.

The voltage-dependent temperature and current profiles of three Ag mesh heaters are given in figure 4(a). The size of the Ag mesh heaters was  $3 \times 4 \text{ cm}^2$ . Voltage was ramped up at a  $1 \text{ V}/100 \text{ s}$  rate. We collected the temperature responses of the heaters every five seconds and current responses every second. We stopped applying the voltage to prevent substrate damage due to high temperature before the temperature of the sample reached  $\sim 100^\circ\text{C}$ . In these experiments, all samples show that, as the applied voltage increased, the temperature and current also increased. However, the slopes of the increases in temperature and current are different due to the sheet resistance of the sample. The final voltages varied depending on the sheet resistance of the Ag mesh. For example, for the  $20 \Omega \text{sq}^{-1}$  Ag mesh, the temperature reached  $100^\circ\text{C}$  when the voltage increased to 10 V over 1000 s. In contrast, for the  $300 \Omega \text{sq}^{-1}$  sample, the temperature reached  $90^\circ\text{C}$  when the voltage was increased to 23 V over 2300 s. The heater composed of a  $20 \Omega \text{sq}^{-1}$  Ag mesh exhibited better



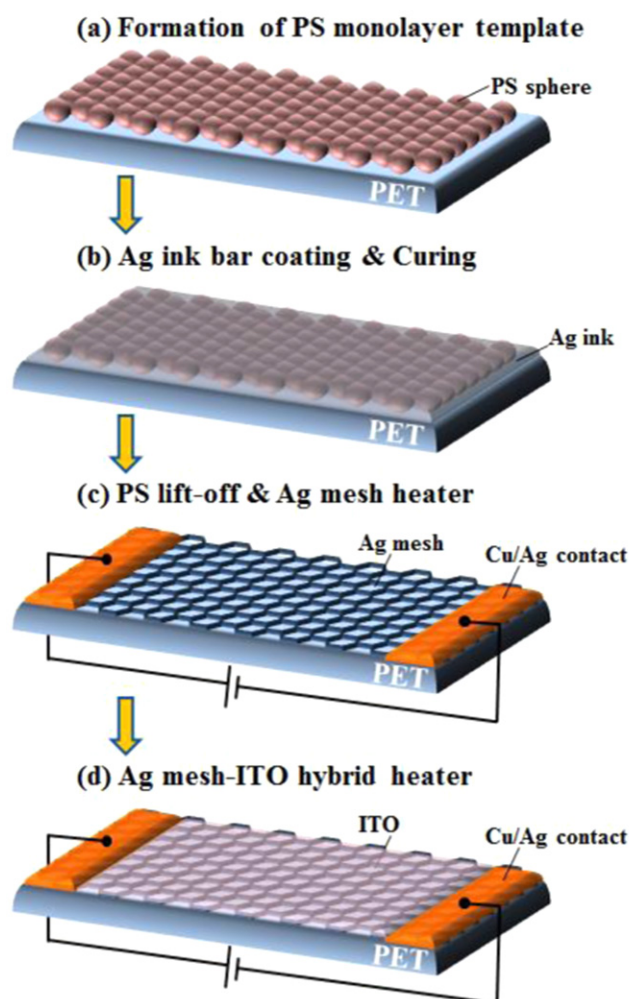


**Figure 2.** Schematic processes used to fabricate an Ag mesh-ITO hybrid heater using a PS sphere monolayer template.

voltage-temperature characteristics compared to those composed of higher-sheet-resistance Ag meshes in terms of the temperature response with respect to the applied voltage. Thus, the electrical conductivity of Ag meshes is a prime factor for achieving better performance in Ag mesh heaters.

The resistances of the aforementioned Ag meshes based on I-V curves were estimated to be  $26.4 \Omega$ ,  $56.6 \Omega$ , and  $287.5 \Omega$  for the  $20 \Omega \text{ sq}^{-1}$ ,  $100 \Omega \text{ sq}^{-1}$ , and  $300 \Omega \text{ sq}^{-1}$  meshes, respectively. The power consumptions of Ag mesh heaters can also be obtained from the calculation using basic electrical formulas ( $P [\text{W}] = I^2 R = V^2 / R$ ), where  $P$  is the total power consumption,  $R$  is the resistance of the operating Ag mesh heater,  $V$  is the applied voltage, and  $I$  is the current passing through the Ag mesh heater. Saturation temperature as a function of the power was plotted in figure 4(b). The linear relationships between the power consumption and the saturation temperature were observed from figure 4(b), where the power consumption was calculated based on theoretical and experimental data. The power consumption of the Ag mesh heater at about  $93^\circ\text{C}$  is  $17.8 \text{ W mm}^{-2}$ ; this is quite similar to that of the graphene heater reported by Hong's group, where the power consumption of the graphene heater

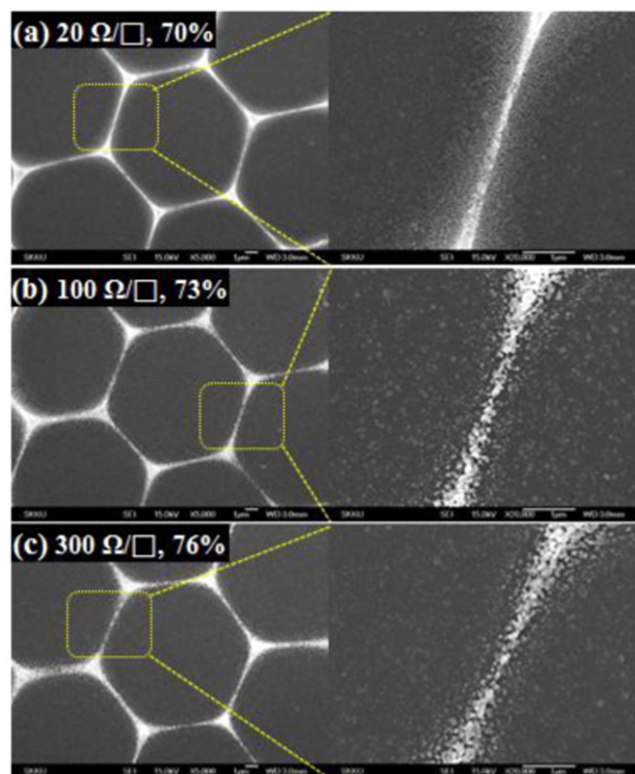


**Figure 3.** FE-SEM images obtained from wet-etched Ag honeycomb meshes: (a)  $20 \Omega \text{ sq}^{-1}$  and 70%, (b)  $100 \Omega \text{ sq}^{-1}$  and 73%, and (c)  $300 \Omega \text{ sq}^{-1}$  and 76%.

**Table 1.** Summarised properties of Ag meshes obtained using the wet etching process.

Sample	Transmittance (%)	Sheet resistance ( $\Omega \text{ sq}^{-1}$ )
Ag mesh sample 1	70	20
Ag mesh sample 2	73	100
Ag mesh sample 3	76	300

at  $95^\circ\text{C}$  was  $20.3 \text{ W mm}^{-2}$  [11]. In contrast, the power consumption of the ITO heater ( $\sim 392 \Omega \text{ sq}^{-1}$ ) at  $31^\circ\text{C}$  was estimated to be  $3.63 \text{ W mm}^{-2}$ . The calculated power consumption of the Ag mesh heater ( $300 \Omega \text{ sq}^{-1}$ ) at the same temperature ( $31^\circ\text{C}$ ) is  $\sim 1.42 \text{ W mm}^{-2}$ , which is half of that of an ITO-based heater. That is, the power consumption efficiency of the Ag mesh heater is outstanding because of the higher electrical conductivity of silver than that of ITO. The inset of figure 4(b) depicts an infrared thermal image of the Ag mesh film ( $20 \Omega \text{ sq}^{-1}$ ) at a saturated temperature (about  $40^\circ\text{C}$ ) under 4 V. The temperature distribution of the Ag mesh heater appears relatively uniform.

Rise and decay characteristics in the temperature of the heater are important features for characterizing the heater in terms of the response to the applied voltage. In an effort to examine the stability and reliability of the Ag mesh heater, a

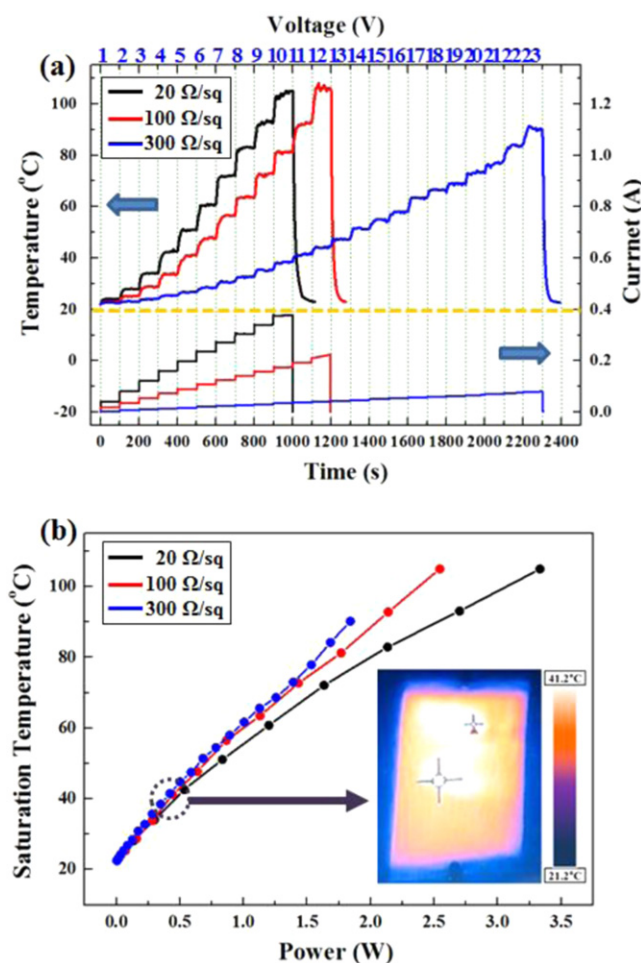


**Figure 4.** (a) Voltage-dependent temperature and current profiles of three types of Ag mesh heaters ( $20$ ,  $100$ , and  $300 \Omega \text{ sq}^{-1}$ ). (b) Relationship between input power and saturated temperature of Ag mesh heaters. The inset is an infrared thermal image of the Ag mesh film ( $20 \Omega \text{ sq}^{-1}$ ) at the steady-state temperature of  $40^\circ\text{C}$ .

heat cycling test was performed. The experimental results performed over 10 cycles (turn-on for 200 s and turn-off for 50 s) are shown in figure 5(a). The tests were done at the same temperature ( $40^\circ\text{C}$ ) for all samples. The required voltages were different due to the difference in the sheet resistances of the samples given in figure 4(a). As shown, 4 V was required to reach  $40^\circ\text{C}$  for the smallest sheet resistance sample ( $20 \Omega \text{ sq}^{-1}$ ), whilst 11 V was required to reach the same temperature for the largest sheet resistance sample ( $300 \Omega \text{ sq}^{-1}$ ). On the other hand, 5 V was required to reach  $40^\circ\text{C}$  for the other sheet resistance sample ( $100 \Omega \text{ sq}^{-1}$ ). Thus, it was determined that the saturated temperature depends on the conductivity of the sample. As shown in figure 5(a), the temperatures of the samples initially increased sharply when the voltages were applied and then reached the saturated temperature. Saturated temperatures were reached within 40 s, thereby resulting in a uniform heat distribution everywhere. The response time, which is defined as the time to reach a steady-state temperature from room temperature, was not considerably affected by the sheet resistance of the sample [10]. In the same manner, when the applied voltage

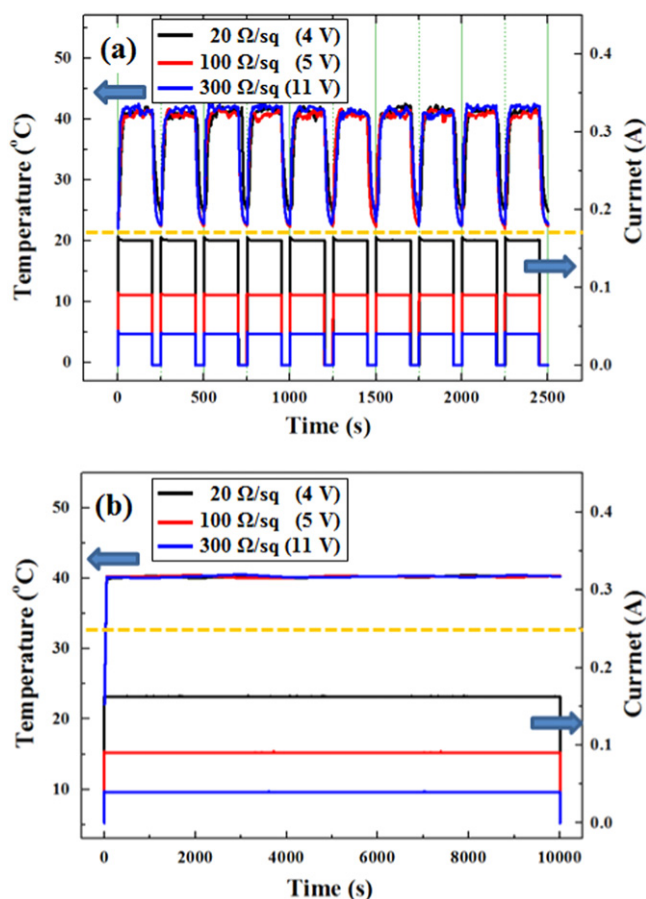


**Figure 5.** Stability and reliability tests of the Ag mesh heaters. (a) Temperature and current response behaviours of the Ag heaters for 10 cycles. (b) Temperature stability of the heater for 10 000 s.

was removed, the temperature decreased more quickly. For a cycling test, temperatures were reached at the same saturated temperature during turn-on cycles, and temperature responses were similar without a noticeable change during turn-off cycles. The long-term stabilities of the film heaters are shown in figure 5(b). There was no significant change in the temperature and the current for 10 000 s, resulting in a uniform heat distribution and good stability.

### 3.3. Ag mesh-ITO hybrid heater

In general, it is possible to improve the transmittance of Ag mesh by wet etching [21]. However, wet etching causes a degradation of the electrical conduction due to the sharp increase in the sheet resistance of Ag mesh. An Ag mesh sample with a transmittance of 90% was obtained by wet etching. FE-SEM images and scanning probe microscopy (SPM) topologies with analysed thickness profiles are shown in figure 6. Through these data, the width and thickness of Ag lines were obtained by averaging over 12 data sets and summarized as shown in table S1. As shown in figures 6(a), (b), the FE-SEM image of the Ag mesh after wet etching is quite different from that prior to wet etching. After wet etching, the lines of Ag meshes became thinner and broke at the central regions, as shown in the enlarged image given in



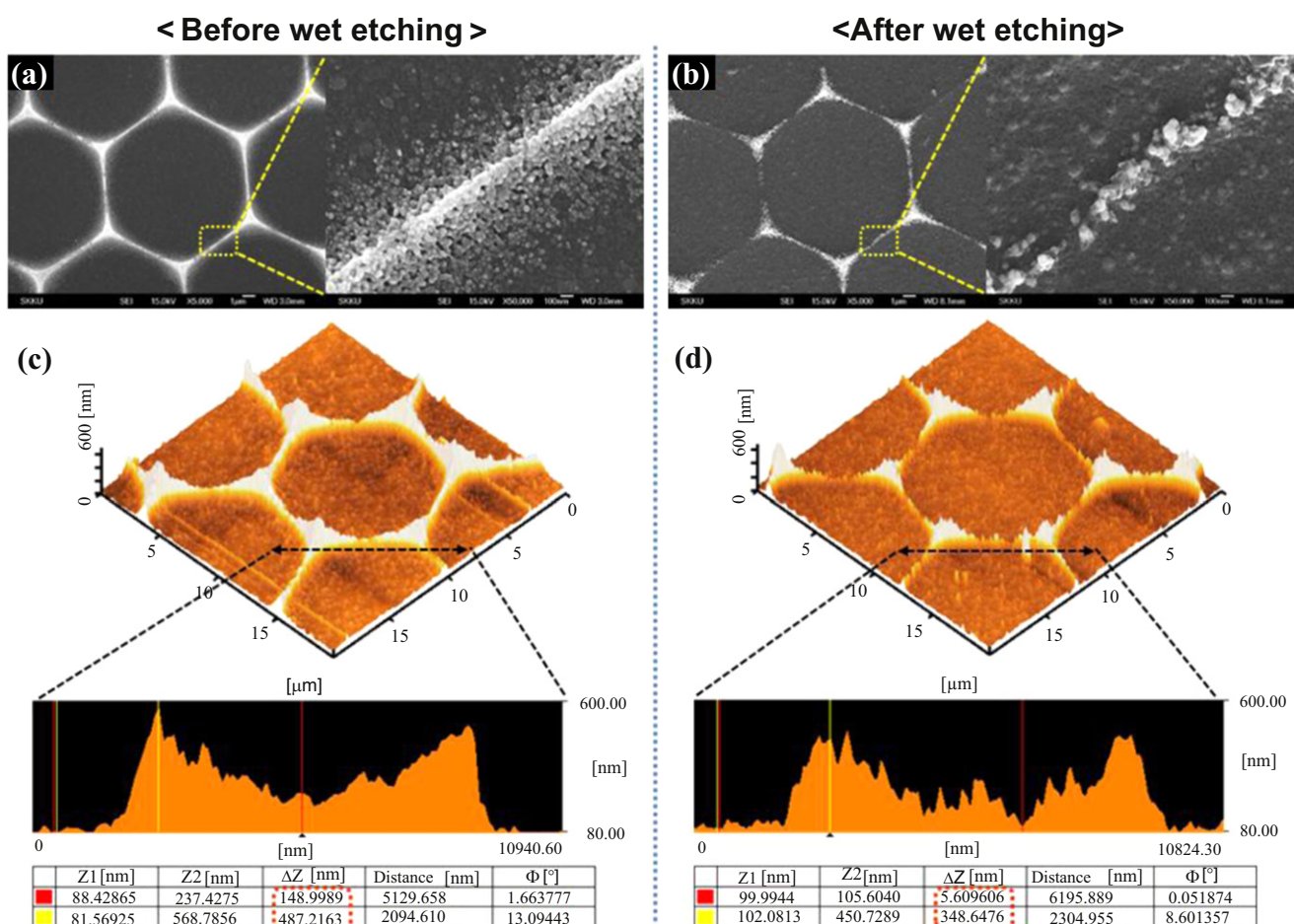


**Figure 6.** FE-SEM images and SPM topologies of Ag meshes: (a) FE-SEM images of Ag mesh before wet etching, (b) FE-SEM images of Ag mesh after wet etching to yield 90% transmittance, (c) 3D SPM image with thickness profile of Ag mesh before wet etching, (d) 3D SPM image with thickness profile of Ag mesh after wet etching to yield 90% transmittance.

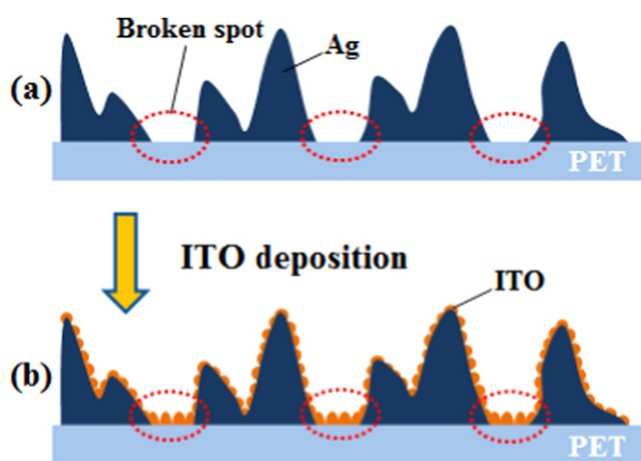


**Figure 7.** Schematic cross-sectional images (a) before ITO deposition on a broken Ag line (b) after ITO deposition on a broken Ag line.

figure 6(b). As shown in table S1., the width of the Ag lines before wet etching was  $798.8 \pm 101.8$  nm, while that of Ag lines after wet etching was  $232.3 \pm 21.2$  nm. The larger reduction in the width of Ag lines is attributed to the

existence of thin parasitic Ag islands near Ag lines. As the wet etching was carried out, Ag parasitic islands having lower thickness were removed easily. This large reduction of Ag line width increased transmittance from 70% to 90%. The topology image obtained using SPM indicates that the thickness of the Ag line in the central region is thinner than those at other regions. A detailed thickness profile given in figure 6(c) shows that the thickness of the Ag line in the central region is  $177.1 \pm 41.3$  nm, which is one-third of the thickness of the highest spot ( $469.8 \pm 37.9$  nm). After wet etching, the thickness of Ag lines at the central region and vertex region are  $41.7 \pm 29.1$  nm and  $364.5 \pm 20.2$  nm, respectively. It indicates that Ag lines in the central region would be easily broken during wet etching. Thus, some broken spots of Ag lines were found from the FE-SEM and SPM images obtained from the wet-etched Ag mesh, as shown in figure 6(d). The non-conductive behaviour of Ag mesh after wet etching to obtain 90% transmittance resulted from such broken lines in Ag meshes. A detailed analysis based on the FE-SEM image and thickness profile shows that the gaps between broken Ag lines ranged from approximately 50 nm to 200 nm. Such non-conductive behaviour due to the wet etch can be solved by depositing a

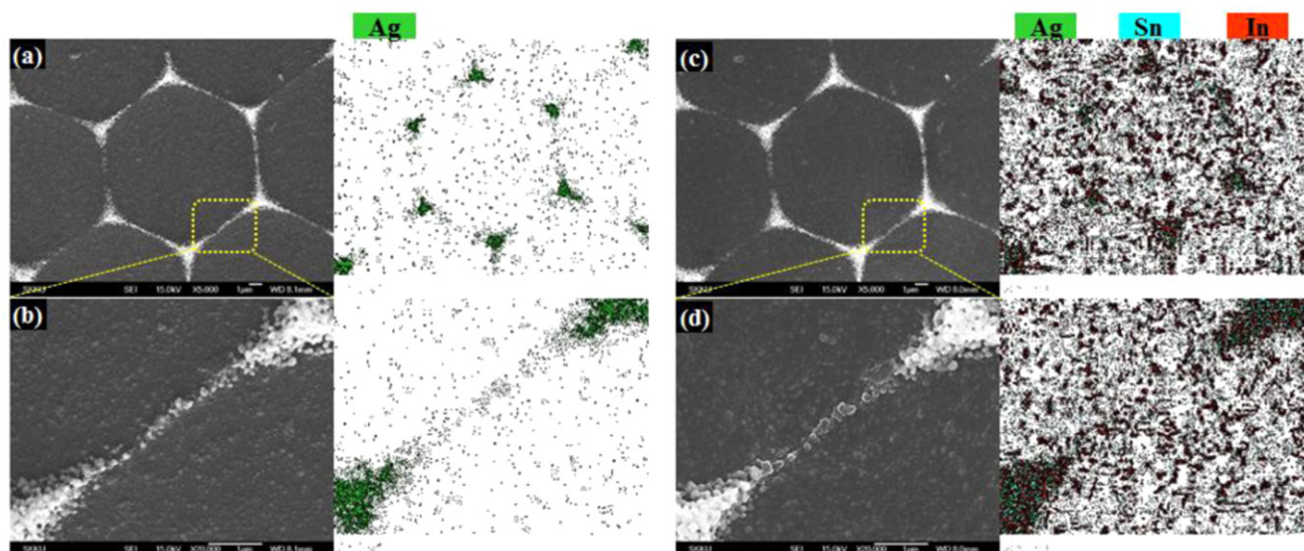


**Figure 8.** FE-SEM images and their EDS mapping images of Ag mesh (T=90%) in the same spot (a) before ITO deposition, (b) magnified images of (a) and (c) after ITO deposition, and (d) magnified images of (c).

finite amount of ITO on the wet etched sample. That is, ITO nano-particles could act as a bridge to connect broken Ag lines through ITO deposition on over-etched Ag mesh samples. Figure 7 shows the schematic cross-sectional images to represent before and after ITO deposition on broken Ag lines. As shown in figure 7(a), there are broken spots between Ag lines after long durations of wet etching. After the ITO deposition given in figure 7(b), ITO nano-particles exist between broken Ag lines, and they connect the broken Ag lines, thereby improving the electrical conduction of the etched Ag mesh sample. A similar study on hybrid films using Ag and ITO was performed to improve conductivity of ITO films by embedding Ag thin films into ITO layers [16, 17]. Even though the materials were the same, the structure of the hybrid films was different. They used ITO films as a major material, and Ag thin films were embedded between ITO films like a sandwich structure, whilst we used ITO as a minor material to connect broken Ag lines of mesh to improve conductivity. Our approach was to maximise the transmittance of the Ag mesh using wet etching and then to improve the conductivity of etched Ag mesh through a minimal ITO overcoat. Thus, it was necessary to understand the property variation of ITO films in terms of ITO thickness.

We examined sputtered ITO films in terms of the ITO thickness. As the ITO thickness increased, the electrical conductance also increased, whilst the transmittance decreased. Therefore, we needed to determine the optimised ITO thickness by a compromise between the transmittance and the conductance. The best result we expected was to fill the aforementioned gaps to connect Ag lines with ITO grains without serious losses in transmittance. To determine the property variation of the ITO layer in terms of ITO thickness, ITO films with four different thicknesses (50, 20, 15, and 10 nm) were deposited on bare PET. The properties of the ITO films, including transmittance, sheet resistance,

resistivity, and grain size are summarised in table 2. In addition, the transmittance and the calculated resistivity were plotted as a function of the ITO thickness in figure S2. As shown, the resistivity decreases linearly with respect to the thickness of ITO as the thickness of ITO increases from 15 nm to 50 nm. However, the resistivity of ITO abruptly increased when the thickness of ITO was 10 nm. These values of ITO film resistivity and their dependence on thickness were in good agreement with previous results [23–25]. Han *et al* reported that there had been five steps in the electrical conductance of ITO films as a function of ITO thickness [23]. In our case, distinct regions were observed in terms of the variation of the resistivity of ITO films. That is, there was a critical point between 10 nm and 15 nm to distinguish the ITO growth mechanism. In other words, ITO tends to form islands when the thickness is below 10 nm, which enhances the grain boundary scattering due to the lack of a sufficient continuous layer. The transition from island growth to layered growth takes place at thicknesses between 10 nm and 15 nm. Surface morphologies of the aforementioned four ITO films on bare PET are shown in figure S3. Nano-scaled grains below 10 nm were observed on the surface of both 20 nm ITO films and 15 nm ITO films. On the other hand, grains with sizes of 10 nm to 30 nm were visible from ITO films 50 nm thick. In particular, it was difficult to find ITO grains from ITO films 10 nm thick, which indicates why the resistivity of ITO abruptly increased at that boundary in the thickness of ITO. As expected, we found that the grain sizes of the ITO film increase as the thickness of the ITO film increases, which is consistent with a previously reported study [24]. As shown in figure S2 and table 2, even though 50 nm ITO can slightly improve the conductivity (39%) compared with that of 15 nm ITO, it loses the transmittance noticeably (8%). On the contrary, 10 nm ITO suffers seriously in the conductivity (42%) with respect to 15 nm ITO, while the transmittance is not improved noticeably. The thickness of 15 nm was the



**Table 2.** Summarised properties of ITO films as a function of ITO thickness.

ITO thickness (nm)	Transmittance (%)	Sheet resistance ( $\Omega \text{ sq}^{-1}$ )	Resistivity ( $\Omega \text{ cm}$ )	Grain size(nm)
50 nm	90	100	$5.0 \times 10^{-4}$	10–30
20 nm	97	400	$8.0 \times 10^{-4}$	<10
15 nm	98	550	$8.3 \times 10^{-4}$	<10
10 nm	98	1400	$1.4 \times 10^{-3}$	—

optimized result, which presented the high transmittance without losing conductivity seriously. That is the reason we selected 15 nm ITO rather than 50 nm ITO. As a result, we chose 15 nm as an optimised thickness as a compromise between higher transmittance and lower resistivity.

We fabricated hybrid Ag meshes combined with ITO thin films. At first, we prepared Ag mesh samples with three different transmittances (84, 87, and 90%) using wet etching. Then, we deposited 15 nm thick ITO on the samples. Figure 8 provides detailed FE-SEM images and EDS mapping images obtained before and after ITO deposition on Ag mesh, the transmittance of which is 90%. SEM images were obtained at the same spots of the Ag mesh in order to compare before and after ITO deposition. In addition, EDS detecting parameters, such as time, applied voltage, and current, were maintained at the same conditions. The FE-SEM image and EDS mapping image of the Ag mesh before ITO deposition are given in figure 8(a), which shows that Ag lines in the central region were broken. Thus, the silver signal given in the EDS mapping image was not detected in that region. Such an observation was further supported from the enlarged images given in figure 8(b). FE-SEM images and EDS mapping images obtained after depositing 15 nm ITO were given in figures 8(c), (d) and are compared to those obtained before ITO deposition. ITO grains were found from FE-SEM images at both the Ag mesh and PET substrate. In particular, as shown in the EDS mapping image, tin and indium signals were detected in the gap between broken Ag lines over all parts of the surface. This indicates that ITO grains connected broken Ag lines, thereby forming an Ag mesh-ITO hybrid conductive film. The measured sheet resistance of the hybrid Ag mesh was  $300 \Omega \text{ sq}^{-1}$ . Furthermore, the sheet resistance of 15 nm ITO was  $550 \Omega \text{ sq}^{-1}$ . That is, the resistivity of 15 nm ITO was  $8.3 \times 10^{-4} \Omega \text{ cm}$ , whilst that of the Ag mesh was  $4.2 \times 10^{-6} \Omega \text{ cm}$ . Thus, the reduction in sheet resistance of the Ag mesh-ITO hybrid film is attributed to the electrical conductivity difference between Ag and ITO. This indicates that most current flows through Ag lines rather than ITO because of the difference in conductivity. Furthermore, current only flows through ITO at the bridges where ITO grains connected between broken Ag lines. The origin of the conductivity degradation in the Ag mesh-ITO hybrid is explained by the existence of ITO grains in the serial network. FE-SEM and EDS images of Ag mesh samples ( $T=84$  and  $87\%$ ) are also shown in figure S4. Due to the shorter etching time, fewer Ag lines were broken, and the gaps between the broken Ag lines were narrower, below 50 nm. In addition, more silver signals were detected from Ag lines of the hexagonal structures from

**Table 3.** Summarised properties of Ag mesh-ITO hybrids obtained by depositing 15 nm of ITO on Ag mesh.

Sample	Transmittance (%)	Sheet resistance ( $\Omega \text{ sq}^{-1}$ )
Before wet etching	70	20
After wet etching	84	>2000
	87	>2000
	90	>2000
After depositing 15 nm of ITO	82	200
Ag mesh	85	250
Ag mesh	88	300
Ag mesh		

EDS mapping images compared to those detected from Ag mesh samples ( $T=90\%$ ).

The deposition of 15 nm ITO resulted in the differences in sheet resistance and transmittance, as summarised in table 3. The transmittances were decreased about 2% after ITO deposition, but the sheet resistances were decreased abruptly, thereby yielding conductive films. Samples with lower transmittances ( $T=84$  and  $87\%$ ) resulted in lower sheet resistances compared to those with higher transmittances ( $T=90\%$ ). As the Ag mesh was increasingly etched, the widths of Ag lines and the number of gaps between broken Ag lines increased. As a result, more ITO bridges existed in the hybrid film after ITO deposition. Thus, the sheet resistance of the hybrid Ag sample with a lower transmittance was lower compared to that obtained from the hybrid Ag sample with higher transmittance.

Finally, we fabricated hybrid Ag meshes coated with various thicknesses of ITO films. At first, we prepared Ag mesh samples with transmittances of 90%, utilizing wet etching. Then, we deposited different thicknesses of ITO layers on the aforementioned samples, where the thicknesses of ITO were 15 nm, 20 nm, and 50 nm. Variations in sheet resistance and transmittance were plotted as a function of ITO thickness in figure 9 for both ITO films and Ag mesh-ITO hybrid meshes. The variations in transmittance are shown in the upper part of the graph, whilst those of sheet resistance are given in the lower part of the graph, in terms of ITO thickness. For ITO films, transmittance and sheet resistance

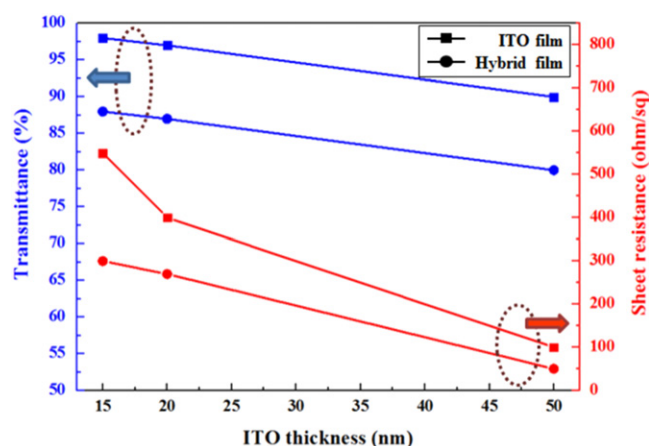


**Figure 9.** Variations in sheet resistance and transmittance as a function of ITO thickness for ITO films and Ag mesh-ITO hybrid films.

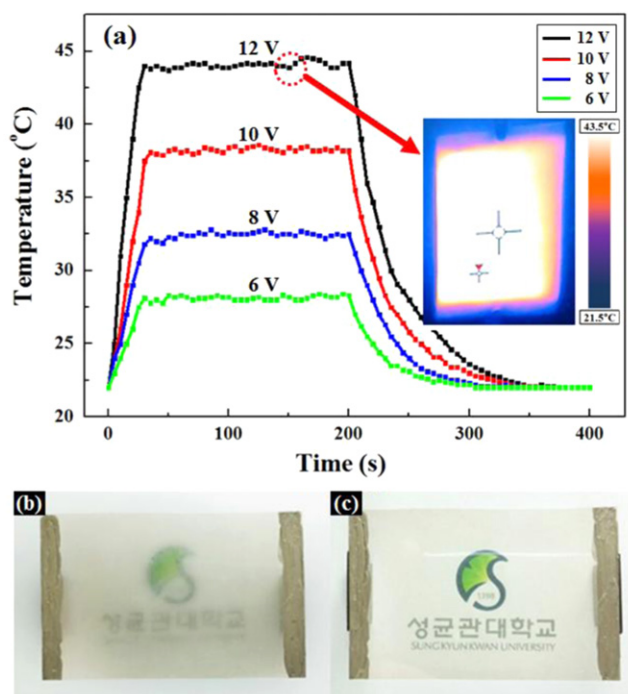


**Figure 10.** (a) Temperature profiles of the Ag mesh-ITO hybrid heater (88% and  $300 \Omega \text{ sq}^{-1}$ ) for different input voltages. The inset is an infrared thermal image of the Ag mesh-ITO hybrid film ( $300 \Omega \text{ sq}^{-1}$ ) at the saturated temperature ( $43^\circ\text{C}$ ). Defrosting test results of Ag mesh-ITO hybrid heater: (b) frosted Ag mesh-ITO hybrid heater (c) defrosted Ag mesh-ITO hybrid heater at 12 V.

decrease as the thickness of ITO increases for both ITO films and hybrid Ag mesh films. Even though the variation trend in transmittance and sheet resistance is similar, the sheet resistance near 15 nm ITO film is noticeable. That is, the thinner ITO deposition below 15 nm is not a good choice for hybrid Ag mesh.

Amongst the various combinations we examined, we selected a  $300 \Omega \text{ sq}^{-1}$  Ag mesh-ITO hybrid with 88% transmittance for the transparent heater. The time-dependent temperature profiles of the aforementioned Ag mesh-ITO

hybrid heater are plotted with respect to the input voltages from 6 V to 12 V with 2 V steps in figure 10(a). When the input voltage was increased to 12 V, the heater temperature reached  $43^\circ\text{C}$ , which could be obtained from the Ag mesh heater ( $88\%$ ,  $300 \Omega \text{ sq}^{-1}$ ) given in figure 4(a). Thus, the same temperature, namely,  $43^\circ\text{C}$  was achieved using an Ag mesh-ITO hybrid without seriously hurting transmittance (2% lost). In addition, the efficiency of power consumption is still good in the Ag mesh-ITO hybrid even though the ITO thin layer had been deposited on the etched Ag mesh. Regardless of the applied voltages, it reached a steady-state temperature within 30 s, which is similar to the results of Ag mesh heaters. The inset of figure 10(a) depicts an infrared thermal image of an Ag mesh-ITO hybrid film ( $300 \Omega \text{ sq}^{-1}$ , 88%) at a steady-state temperature ( $\sim 43^\circ\text{C}$ ) under an applied voltage of 12 V. The temperature distribution of the Ag mesh-ITO hybrid film was highly uniform, based on the colour. In an effort to further demonstrate its potential as an efficient defroster in a vehicle, a defrost test was performed. The aforementioned Ag mesh-ITO hybrid heater ( $300 \Omega \text{ sq}^{-1}$ , 88%) was put into a refrigerator for one hour to allow frost to form on the entire Ag mesh film, which significantly reduced the visibility due to the frost on the heater, as shown in figure 10(b). The frost on the surface was completely removed within 20 s after supplying 12 V to the heater, thereby making the symbol marks and letters in the background clearly visible, as shown in figure 10(c).

Another important application of Ag mesh is as a heating pad on a table during computerised tomography (CT) and x-ray testing. Even though a blanket was offered to patients to maintain body heat, it was not enough to maintain body heat. Heating pads consisting of metal wires like nickel could not be used in these cases due to image interference, as shown in figure S5(a). However, Ag mesh did not appear in the x-ray image, as shown in figure S5(b), and therefore demonstrates great potential to be used as a heat pad in various medical areas.

#### 4. Conclusions

Hybrid TCF heaters were successfully fabricated by depositing a finite ITO on Ag mesh. The optimised ITO thickness was determined by considering the conductance without hurting transmittance, resulting in a thickness of 15 nm. The transmittance of the Ag mesh-ITO hybrid was 88%, and the sheet resistance was  $300 \Omega \text{ sq}^{-1}$ . For the same sheet resistance ( $300 \Omega \text{ sq}^{-1}$ ), transmittance was improved by 12% compared to that of Ag mesh. This result was attributed to the fact that the broken Ag lines of Ag mesh due to etching had been connected by the ITO nano particles, thereby recovering the conductance. Additionally, the power consumption efficiency of the Ag mesh-ITO hybrid heater is much better than that of the ITO based heater. Finally, we demonstrated our Ag mesh-ITO hybrid heater as an efficient vehicle defroster by operating at 12 V, which can be supplied from vehicle batteries.

## Acknowledgments

This research was supported by a grant from the Fundamental R&D Program for Technology of World Premier Materials funded by the Ministry of Knowledge Economy, Republic of Korea.

## References

- [1] Pang S, Hernandez Y, Feng X and Müllen K 2011 *Adv. Mater.* **23** 2779
- [2] Hecht D S, Hu L and Irvin G 2011 *Adv. Mater.* **23** 1482
- [3] Kumar A and Zhou C 2010 *ACS Nano* **4** 11
- [4] Kim T, Kim Y W, Lee H S, Kim H, Yang W S and Suh K S 2012 *Adv. Funct. Mater.* **23** 1250
- [5] Lee J, Connor S T, Cui Y and Peumans P 2008 *Nano Lett.* **8** 689
- [6] MacDiarmid A G 2001 *Angew. Chem. Int. Ed.* **40** 2581
- [7] Vosgueritchian M, Lipomi D J and Bao Z 2012 *Adv. Funct. Mater.* **22** 421
- [8] Kang T J, Kim T, Seo S M, Park Y J and Kim Y H 2011 *Carbon* **49** 1087
- [9] Yoon Y H, Song J W, Kim D, Kim J, Park J K, Oh S K and Han C S 2007 *Adv. Mater.* **19** 4284
- [10] Jung D, Kim D, Lee K H, Overzet L J and Lee G S 2013 *Sens. Actuator A-Phys.* **199** 176
- [11] Kang J, Kim H, Kim K S, Lee S K, Bae S, Ahn J H, Kim Y J, Choi J B and Hong B H 2011 *Nano Lett.* **11** 5154
- [12] Sui D, Huang Y, Huang L, Liang J, Ma Y and Chen Y 2011 *Small* **7** 3186
- [13] De S *et al* 2009 *ACS Nano* **3** 714
- [14] Zhu R *et al* 2011 *ACS Nano* **5** 9877
- [15] Chang H, Wang G, Yang A, Tao X, Liu X, Shen Y and Zheng Z 2012 *Adv. Funct. Mater.* **20** 2893
- [16] Indluru A and Alford T L 2009 *J. Appl. Phys.* **105** 123528
- [17] Guillen C and Herrero J 2009 *Sol. Energy Mater. Sol. Cells* **92** 938
- [18] Kang M and Guo L J 2007 *Adv. Mater.* **19** 1391
- [19] Ho Y, Chen K, Liu S, Chang Y, Huang D and Wei P 2011 *Org. Electron.* **12** 961
- [20] Cheng K, Cui Z, Li Q, Wang S and Du Z 2012 *Nanotechnology* **23** 425303
- [21] Kwon N, Kim K, Sung S, Yi I and Chung I 2013 *Nanotechnology* **24** 235205
- [22] Qi H, Hao W, Xu H, Zhang J and Wang T 2009 *Colloid Polym. Sci.* **287** 243
- [23] Han Y, Kim D, Cho J S, Beag Y W and Koh S K 2006 *Thin Solid Films* **496** 58
- [24] Gao M, Job R, Xue D and Fahrner W R 2008 *Chin. Phys. Lett.* **25** 1380
- [25] Kim D, Park M, Lee H and Lee G 2006 *Appl. Surf. Sci.* **253** 409